

Disks in a narrow channel jammed by gravity and centrifuge: profiles of pressure, mass density and entropy density

Christopher Moore¹, Dan Liu², Benjamin Ballnus³, Michael Karbach³, and Gerhard Müller¹

¹ Department of Physics, University of Rhode Island, Kingston RI 02881, USA

² Department of Physics, University of New Haven, West Haven CT 06516, USA

³ Bergische Universität Wuppertal, Fachbereich C, 42097 Wuppertal, Germany

PACS numbers: 83.80.Fg, 61.43.-j, 64.75.Gh

Abstract. This work investigates jammed granular matter under conditions that produce heterogeneous mass distributions on a mesoscopic scale. We consider a system of identical disks that are confined to a narrow channel, open at one end and closed off at the other end. The disks are jammed by the local pressure in a gravitational field or centrifuge. All surfaces are hard and frictionless. We calculate the profiles of pressure, mass density, and entropy density on a mesoscopic length scale under the assumption that the jammed states are produced by random agitations of uniform intensity along the channel. These profiles exhibit trends and features governed by the balancing of position-dependent forces and potential energies. The analysis employs a method of configurational statistics that uses interlinking two-disk tiles as the fundamental degrees of freedom. Configurational statistics weighs the probabilities of tiles according to competing potential energies associated with gravity and centrifugation. Amendments account for the effects of the marginal stability of some tiles due to competing forces.

1. Introduction

One criterion commonly used to demarcate the granular regime from the colloidal regime in a suspension compares the energy $k_B T$ of thermal fluctuations with the gravitational potential energy $mg\sigma$ of a suspended particle when lifted a distance equal to its diameter σ [1]. It follows that the earth's gravitational field g has a part in terrestrial experiments on granular matter. It can reasonably be argued that the variations with vertical distance of quantities under investigations are undetectably small in a wide range of experiments. Effects of gravity are real and interesting, nevertheless. Jammed macrostates produced via some protocol are described by characteristic profiles of pressure, mass density, entropy density, mechanical coordination numbers etc. Other fields or potentials produce their own profiles in the same quantities. We shall consider combinations of gravity and centrifuge

How are trends and features in these profiles related to particular local configurations of jammed grains? Reliable answers to this wide-ranging question are hard to get in general. Evidence from experimental, theoretical, and computational

studies point to the balances of forces and potential energies that determine the nature of jammed states [2-19].

We shall argue that the balance of relevant forces and the relative sizes of relevant potential energies may affect the profiles in separate ways. To support this argument with evidence that is methodologically sound and, at the same time, transparent regarding its physical origin, we consider a somewhat idealized model: a system of disks confined to a narrow channel.

The work reported here builds on previous studies as described in the following. Ashwin, Bowles, and Saika-Voivod [20, 21, 22] introduced a simple model of rigid disks of one size and mass in a narrow channel. The disks are positioned in a horizontal plane and jammed by a uniform pressure. Two regimes of channel widths were identified, for which the configurations of jammed disks can be described by a finite number of interlinking tiles (four tiles in one regime and 32 tiles in the other). The configurational entropy versus volume fraction was calculated by elementary means in the first regime and by a transfer matrix technique in the second.

Gundlach *et al.* [23] generalized the analysis of the first regime to a channel with its plane oriented vertically and its axis still horizontal. The effects of gravity were shown to produce a critical point at which the system is highly susceptible to ordering tendencies. Criticality was shown to be robust in the presence of some effects of friction. Remarkable analogies between this system of confined disks subject to gravity and a system of hard spheres subject to friction [7, 8, 9, 10, 11, 12] were identified, including the coexistence of domains with different types or degrees of ordering.

Most recently, a system of disks confined to a narrow channel was used to explore the relationship between thermally equilibrated fluid states and mechanically stabilized jammed states, demonstrating new insights that remain relevant for more complex systems [24, 25]. The rigorous analysis of idealized systems such as this often uncover issues and features that transcend their own limitations.

In this work we extend the analysis of disks jammed in a narrow channel to conditions that produce heterogeneous mass distributions on a mesoscopic scale caused by gravity and centrifuge (see Fig. 1). We tilt the axis of the channel into the (vertical) direction of the gravitational field [scenario (i)] and spin the channel about its axis [scenario (iii)]. We rotate the channel in a horizontal plane with its axis oriented radially and its plane oriented horizontally [scenario (ii)] or vertically [scenario (iv)]. Previous studies of the statistical mechanics of jammed granular columns under gravity in heterogeneous macrostates do exist [26-30] and will be discussed in Sec. 7.

The protocol of random agitations employed here is different from the ones implied in Refs. [20, 21, 22, 23]. No piston is needed. Jamming is caused by the gravitational force [scenario (i)], the centrifugal force [scenario (ii)], or a combination of both [scenarios (iii) and (iv)] acting on the disks when the random agitations are stopped suddenly. These forces vary along the channel, depending on the mass density, which itself varies along the channel. In scenarios (iii) and (iv) the mechanically stable tiles sequences depend on the local jamming pressure.

Disks of mass μ and diameter σ are confined to a long channel of width H with $H/\sigma = 1 + \sqrt{3}/4$. This particular width represents the border between the aforementioned regimes [21]. All surfaces are rigid and frictionless. Jammed microstates are described as sequences of two-disk tiles. Successive tiles are interlinked by sharing one disk as illustrated in Fig. 1.

Tiles come in four distinct shapes. Two of them bear the same name (v), the

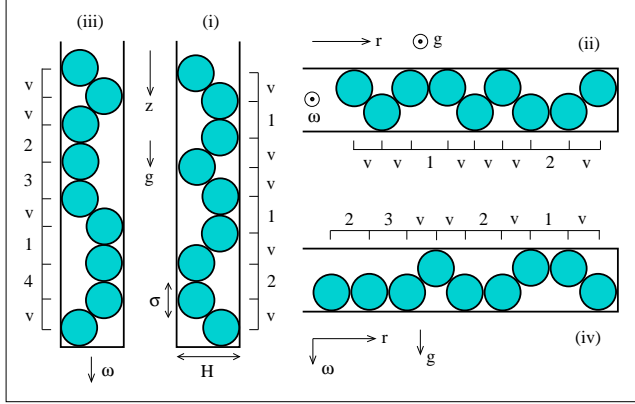


Figure 1. Jammed microstates of disks of mass μ and diameter σ in a channel of width H for scenarios (i)-(iv). For $H/\sigma \leq 1 + \sqrt{3/4}$ all configurations are sequences of interlinking two-disk tiles as shown. In our methodology, tiles v are elements of pseudo-vacuum and tiles 1, 2, 3, 4 are statistically interacting particles.

other two each bear two names, (1,4) and (2,3), respectively, all for a reason. The most compact state is an alternating sequence of tiles v . There is no need to assign different names to the two shapes because all relevant attributes are identical, yet they are not interchangeable.

In scenarios (i) and (ii) the least compact state is a sequence $v \cdots 1v2v1v2 \cdots v$. Here only tiles v can follow each other directly. Any tile 1 (2) is separated from the next tile 1 (2) by at least two tiles v . A tile 1 is separated from the nearest tile 2 by at least one tile v .

In scenario (iii) multiple tiles 1 and multiple tiles 2 following one another directly can be stabilized by the centrifugal force perpendicular to the channel axis at locations where the gravitational pressure is not too strong. Any tile 1 (2) that follows directly another tile 1 (2) is renamed tile 4 (3) in our analysis.

In scenario (iv) tiles 3 but not tiles 4 can be stabilized by the gravitational force perpendicular to the channel axis at locations where the centrifugal pressure is not too strong. Conversely, below a certain threshold centrifugal pressure tiles v and 1 are destabilized by gravity in this scenario.

We describe our methodology in Sec. 2. The next four sections are devoted each to one of the scenarios (i)-(iv) in ascending order of complexity.

2. Statistically interacting tiles

Every jammed microstate is a unique sequence of tiles subject to the rules mentioned. In the absence of acceleration due to gravity/rotation along the channel, jammed macrostates are spatially homogeneous and are fully characterized by the average populations of tiles from each species.

A detailed account of our methodology for such cases can be found in Ref. [23]. The method itself was invented by Haldane [31], and developed by Wu [32], Isakov, [33], Anghel [34], and others [35, 36, 37, 38] in significant aspects. The adaptation

to jammed granular matter as reported in Ref. [23] is embedded in the framework of configurational statistics [39, 40].

Here we extend that account to spatially heterogeneous situations such as caused by gravitational or centrifugal forces. Some aspects of this extension are straightforward, others are more subtle. Many conclusions reached in Ref. [23] remain valid locally for mesoscopic segments of jammed disks.

On any mesoscopic segment of channel we can interpret tiles 1, 2, 3, 4 as statistically interacting quasiparticles excited from the pseudo-vacuum $\mathbf{v}\mathbf{v}\cdots\mathbf{v}$ by random agitations of given intensity in the face of a specific local pressure. The number of distinct segments with given particle content is determined by the multiplicity expression,

$$W(\{N_m\}) = n_{pv} \prod_{m=1}^M \binom{d_m + N_m - 1}{N_m}, \quad (1)$$

$$d_m = A_m - \sum_{m'=1}^M g_{mm'}(N_{m'} - \delta_{mm'}). \quad (2)$$

The pseudo-vacuum has degeneracy $n_{pv} = 2$. The number of particle species is $M = 4$. In the taxonomy of Ref. [36] they belong to the categories host ($m = 1, 2$) and tag ($m = 3, 4$). The capacity constants are $A_1 = A_2 = \frac{1}{2}(N - 1)$ and $A_3 = A_4 = 0$, where N is the number of disks. The statistical interaction coefficients are compiled in Table 1.

Table 1. Statistical interaction coefficients of tiles 1, 2, 3, 4 in the role of quasiparticles.

$g_{mm'}$	1	2	3	4
1	$\frac{3}{2}$	$\frac{1}{2}$	$\frac{1}{2}$	$\frac{1}{2}$
2	$\frac{1}{2}$	$\frac{3}{2}$	$\frac{1}{2}$	$\frac{1}{2}$
3	0	-1	0	0
4	-1	0	0	0

The number of tiles is fixed at $N - 1$. Each \mathbf{v} -tile contributes a volume $\frac{1}{2}\sigma$ and each particle tile twice that. Hence the activation of a particle from any species expands the volume by $\frac{1}{2}\sigma$.

Configurational statistics postulates that jammed macrostates with specific profiles of mass density and entropy density can be generated reproducibly via sufficiently well-defined protocols of random agitations. Our calculations assume a protocol in which the random agitations of controlled intensity are applied uniformly along the channel. When these agitations are stopped abruptly, a jammed microstate is frozen out in short order by the local gravitational or centrifugal pressure.

The associated jammed macrostate is then characterized by the (dimensionless) parameter field,

$$\hat{p} \doteq \frac{p(x)\sigma}{2T_k}, \quad (3)$$

where $p(x)$ is the local pressure and T_k some measure for the intensity of (uniform) random agitations. We specify the position along the channel by coordinate x

generically. In applications we use z if the axis is vertical and r if it is horizontal and rotating (see Fig. 1).

In scenarios (iii) and (iv) the jammed macrostate also depends on a second (dimensionless) parameter, which is not a field:

$$\hat{\omega}^2 \doteq \frac{\mu\omega^2 d\sigma}{4T_k}, \quad \hat{g} \doteq \frac{\mu g d}{T_k}, \quad (4)$$

respectively, where $d = \frac{1}{2}(H - \sigma) = (\sqrt{3}/4)\sigma$ is half the shortest distance a disk can move between walls. Moreover, in scenarios (i), (iii) with gravitational pressure and (ii), (iv) with centrifugal pressure we use, respectively, scaled position coordinates,

$$\hat{z} \doteq \frac{2\mu g z}{T_k}, \quad \hat{r} \doteq r \sqrt{\frac{\mu\omega^2}{T_k}}. \quad (5)$$

Note that the ω in (4) describes a channel spinning about its axis and the ω in (5) a channel with its axis rotating.

Key relations from the statistical mechanical analysis [23] adapted to heterogeneous situations are a set of linear equations for the scaled tile population densities $\bar{N}_m(x) \doteq \langle N_m(x) \rangle / N$,

$$w_m(x)\bar{N}_m(x) + \sum_{m'=1}^M g_{mm'}\bar{N}_{m'}(x) = \bar{A}_m, \quad (6)$$

where $\bar{A}_m \doteq A_m/N$, and where the $w_m(x)$ are real, non-negative solutions of the nonlinear equations,

$$e^{K_m(x)} = [1 + w_m(x)] \prod_{m'=1}^M [1 + w_{m'}(x)]^{-g_{m'm}}. \quad (7)$$

The $K_m(x)$ will be derived from (3)-(5) case by case. Our focus is on the profiles of the mass density,

$$\tilde{\rho} = \frac{\sigma}{2\mu}\rho(x) = \left[1 + \sum_{m=1}^M \bar{N}_m(x)\right]^{-1}, \quad (8)$$

and the entropy density,

$$\begin{aligned} \bar{S}(x) = \sum_{m=1}^M \left[\left(\bar{N}_m(x) + \bar{Y}_m(x) \right) \ln \left(\bar{N}_m(x) + \bar{Y}_m(x) \right) \right. \\ \left. - \bar{N}_m(x) \ln \bar{N}_m(x) - \bar{Y}_m(x) \ln \bar{Y}_m(x) \right], \end{aligned} \quad (9)$$

$$\bar{Y}_m(x) \doteq \bar{A}_m - \sum_{m'=1}^M g_{mm'}\bar{N}_{m'}(x), \quad (10)$$

in addition to that of pressure $p(x)$. One additional relation is necessary for closure. The local pressure (3), which enters (7) on the left, depends on the profile of mass density (8) in a way that varies between scenarios. This relation will be introduced case by case.

3. Gravity

In scenario (i) the axis of the channel is oriented vertically (see Fig. 1). Tiles 3 and 4 are mechanically unstable against the slightest intensity of random agitations. They do not exist in jammed microstates produced by our protocol. Configurational statistics can accommodate this kind of mechanical instability by simply freezing out tiles 3 and 4. Taking the limit $K_3, K_4 \rightarrow \infty$ leaves Eqs. (6), (7), and (9)-(10) valid for tiles 1 and 2. A further simplification follows from symmetry: tiles 1 and 2 occur with equal probability. We have

$$K_1 = K_2 = \hat{p}, \quad (11)$$

in generalization of the zero-gravity situation [23]. Equations (7) with (11) used on the left are valid on a mesoscopic scale with the z -axis pointing vertically down and $z = 0$ located at the top of the pile of disks. Anghel's rules [34] permit a type-1 merger [38] $1 \& 2 \rightarrow \bar{1}$. Symmetry dictates that $w_1 = w_2 \doteq w$ and $\bar{N}_1 = \bar{N}_2 \doteq \frac{1}{2}\bar{N}$.

The population profile of tiles 1 and 2 combined inferred from Eqs. (6) and (7) depends on the pressure profile as follows:

$$\bar{N} = [w + 2]^{-1}, \quad w = \frac{1}{2}e^{\hat{p}} \left[1 + \sqrt{1 + 4e^{-\hat{p}}} \right]. \quad (12)$$

The local pressure is caused by the weight of the disks piled on top. It depends on the mass density (8) transcribed into

$$\tilde{\rho} = \frac{1}{1 + \bar{N}}, \quad (13)$$

via the integral,

$$p(z) = g \int_0^z dz' \rho(z'), \quad (14)$$

which we invert into

$$\hat{z} = 2 \int_0^{\hat{p}} d\hat{p}' [1 + \bar{N}(\hat{p}')] . \quad (15)$$

The integral yields

$$e^{\hat{z}} = e^{3\hat{p}} \frac{\sqrt{5} + 1}{\sqrt{5} - 1} \frac{\sqrt{1 + 4e^{-\hat{p}}} - 1}{\sqrt{1 + 4e^{-\hat{p}}} + 1}. \quad (16)$$

The entropy density (9)-(10) for this case becomes

$$\bar{S} = \left[(1 - \bar{N}) \ln(1 - \bar{N}) - \bar{N} \ln \bar{N} - (1 - 2\bar{N}) \ln(1 - 2\bar{N}) \right]. \quad (17)$$

Expressing (16) as a cubic equation,

$$(h^2 - 1)(h + 1) = 4(1 + \sqrt{5})e^{-\hat{z}/2}, \quad (18)$$

in $h(\hat{p}) \doteq \sqrt{1 + 4e^{-\hat{p}}}$, we find a unique real solution with asymptotics,

$$h = \begin{cases} \sqrt{5} - \frac{1 + 3\sqrt{5}}{22}\hat{z} + O(\hat{z}^2), & \hat{z} \ll 1 \\ 1 + (1 + \sqrt{5})e^{-\hat{z}/2} + O(e^{-\hat{z}}), & \hat{z} \gg 1 \end{cases}. \quad (19)$$

The curve of $\hat{p} - \frac{1}{2}\hat{z}$ versus \hat{z} in Fig. 2 represents the (negative) deviation from hydrostatic pressure of close-packed disks. Also shown are the pressure asymptotes near the top of the stack and deep down in the channel.

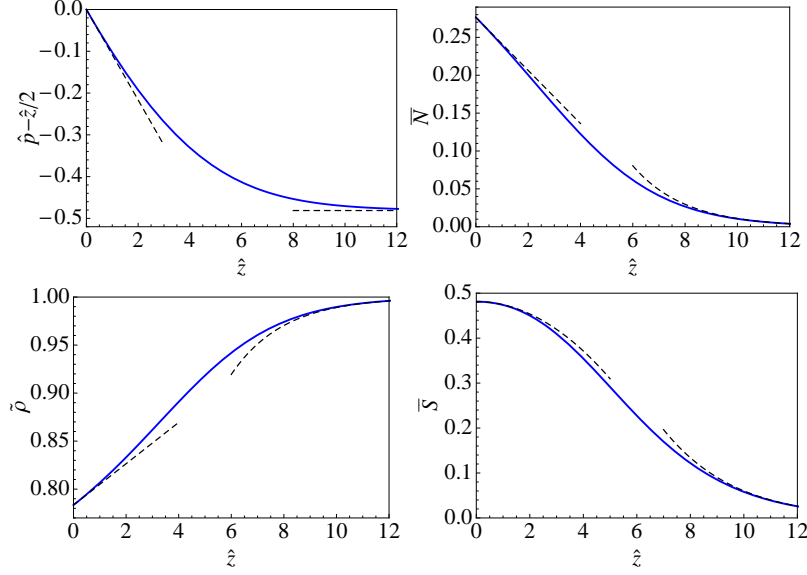


Figure 2. Profiles of scaled pressure, \hat{p} , scaled population density of particle tiles \tilde{N} , scaled mass density $\tilde{\rho}$, and scaled entropy \tilde{S} versus scaled depth \hat{z} in scenario (i). The asymptotics are shown dashed.

The pressure has a universal profile in the scaled variables with asymptotics,

$$\hat{p} = \begin{cases} \frac{15 + \sqrt{5}}{44} \hat{z} + O(\hat{z}^2), & \hat{z} \ll 1 \\ \frac{\hat{z}}{2} - \text{Arcoth}\sqrt{5} + O(e^{-\hat{z}/2}), & \hat{z} \gg 1 \end{cases}. \quad (20)$$

The actual pressure p at actual depth z does, of course, depend on the intensity T_k of random agitations used in our jamming protocol. The overall pressure deep down decreases with increasing T_k as expected.

That same solution enters the expression for the particle population density and the mass density as follows:

$$\tilde{N} = \frac{h(\hat{p}) - 1}{2h(\hat{p})}, \quad \tilde{\rho} = \frac{2h(\hat{p})}{3h(\hat{p}) - 1}. \quad (21)$$

The variation of both densities versus scaled depth as depicted in Fig. 2 is linear near the top and exponential deep down. The asymptotics are

$$\tilde{\rho} = \begin{cases} \frac{2\sqrt{5}}{3\sqrt{5}-1} + \frac{4}{(3\sqrt{5}-1)^3} \hat{z} + O(\hat{z}^2), & \hat{z} \ll 1 \\ 1 - \frac{\sqrt{5}+1}{2} e^{-\hat{z}/2} + O(e^{-\hat{z}}), & \hat{z} \gg 1 \end{cases}, \quad (22)$$

$$\tilde{N} = \begin{cases} \frac{\sqrt{5}-1}{2} - \frac{1+3\sqrt{5}}{5 \cdot 44} \hat{z} + O(\hat{z}^2), & \hat{z} \ll 1 \\ \frac{\sqrt{5}+1}{2} e^{-\hat{z}/2} + O(e^{-\hat{z}}), & \hat{z} \gg 1 \end{cases}, \quad (23)$$

The rate at which $\tilde{\rho}$ grows with depth first increases then decreases toward zero.

The profile of the entropy density inferred from (17), (21), and the physical solution of (18) has the compact form

$$\bar{S} = \text{Arsinh} \left(\frac{1}{2} e^{\hat{p}/2} \right) - \frac{\hat{p}}{2h(\hat{p})}. \quad (24)$$

The asymptotic expansions in terms of \hat{z} are

$$\bar{S} = \begin{cases} \ln \frac{1+\sqrt{5}}{2} - \left(\frac{1+3\sqrt{5}}{44} \right)^2 \frac{\hat{z}^2}{2\sqrt{5}} + O(\hat{z}^3), & \hat{z} \ll 1 \\ \frac{1+\sqrt{5}}{2} \left(\frac{\hat{z}}{2} + 1 - \ln \frac{1+\sqrt{5}}{2} \right) e^{-\hat{z}/2} + O(e^{-\hat{z}}), & \hat{z} \gg 1. \end{cases} \quad (25)$$

It is a monotonically decreasing function as shown in Fig. 2, with a quadratic dependence on \hat{z} near the top and an exponential tail deep down.

Spinning the vertical channel about its axis stabilizes tiles 3 and 4 at sufficiently low gravitational pressure. How this affects the four profiles of Fig. 2 will be discussed in Sec. 5.

4. Centrifuge

Scenario (ii) considers a channel with plane and axis oriented horizontally, rotating with constant angular velocity ω in the horizontal plane (see Fig. 1). All densities are now functions of the radial coordinate r . The disks are jammed by the local pressure due to centrifugation.

Only tiles 1 and 2 are stable and the same symmetries obtain as in scenario (i). Equations (11)-(13) and (17) remain valid whereas Eqs. (14) and (15) are to be replaced, respectively, by

$$p(r) = \omega^2 \int_0^r dr' r' \rho(r'), \quad (26)$$

$$\hat{r}^2 = 2 \int_0^{\hat{p}} d\hat{p}' [1 + \bar{N}(\hat{p}')]. \quad (27)$$

We assume that the column of disks just reaches the location of the axis of rotation. This is a convenient albeit somewhat artificial boundary condition. It preserves all features of interest and avoids clutter. The resulting centrifugal pressure profile reads

$$e^{\hat{r}^2} = e^{3\hat{p}} \frac{\sqrt{5}+1}{\sqrt{5}-1} \frac{\sqrt{1+4e^{-\hat{p}}}-1}{\sqrt{1+4e^{-\hat{p}}}+1}. \quad (28)$$

The four profiles shown in Fig. 3 differ from those shown in Fig. 2 in ways that are as significant physically as they are obvious mathematically. Linear (quadratic) dependences at small \hat{z} are replaced by quadratic (quartic) dependences at small \hat{r} . Exponential behavior at large \hat{z} is replaced by Gaussian behavior at large \hat{r} .

These simple and smooth profiles for a rotating channel will acquire additional structures when the plane is turned from a horizontal into a vertical direction. In that case the mechanical stability of some tiles depends on the centrifugal pressure. The four profiles thus modified will be discussed in Sec. 6.

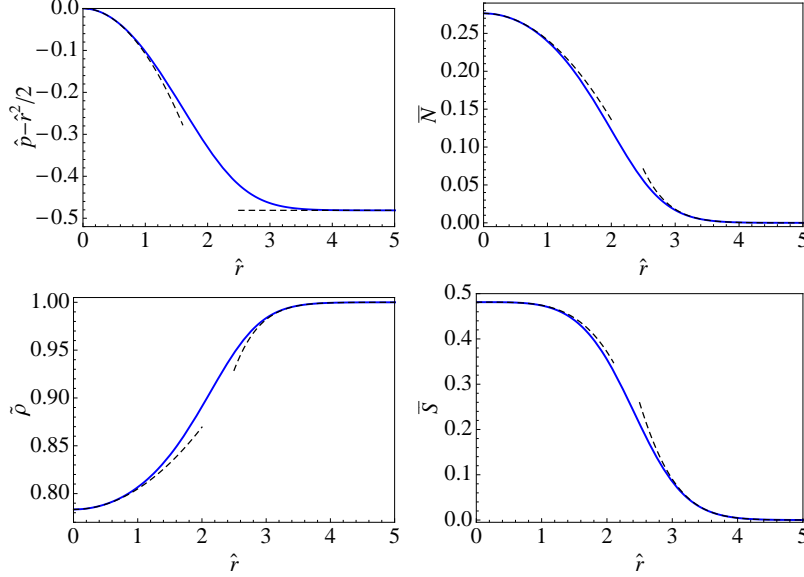


Figure 3. Profiles of scaled pressure \hat{p} , scaled population density of particle tiles \bar{N} , scaled mass density $\bar{\rho}$, and scaled entropy \bar{S} versus scaled radius \hat{r} in scenario (ii). The asymptotics are shown dashed.

5. Gravity with centrifuge

Scenario (iii) is an extension of scenario (i). The channel is spinning about its vertical axis with constant angular velocity ω (see Fig. 1). The spinning has the effect of mechanically stabilizing tiles 3 and 4 provided the local gravitational pressure is not too high.

In all jammed states every disk touches a wall. Hence each disk experiences the same centrifugal force irrespective of what tile it is part of. Only disks that have both neighbors touching the wall on their side need the centrifugal force for their own mechanical stability. All such disks belong to a tile 3 or 4.

Tiles ν , 1, 2 are stable for any pressure. The stability of tiles 3 and 4 is precarious at all nonzero pressures but to varying degrees. Near the top there exists an asymptotic low-pressure regime where tiles 3 and 4 are no less stable than tiles 1 and 2. Deep down there exists an asymptotic high-pressure regime where tiles 3 and 4 are highly unstable. The physics of the two asymptotic regimes is firmly grounded in configurational statistics.

5.1. Low pressure and high pressure

The analysis for the low-pressure asymptotic regime proceeds parallel to that of Sec. 3 with some modifications. We must replace Eq. (11) by

$$K_m = \hat{p}, \quad m = 1, \dots, 4. \quad (29)$$

Before we solve Eqs. (6) and (7) for $M = 4$ statistically interacting particles we take advantage of the symmetries reflected in (29) and in the $A_m, g_{mm'}$ from Table 1.

According to Anghel's rules [34, 38] we can implement three successive mergers,

$$3 \ \& \ 4 \rightarrow \bar{3}, \quad 1 \ \& \ 2 \rightarrow \bar{1}, \quad \bar{1} \ \& \ \bar{3} \rightarrow \bar{1}, \quad (30)$$

that lead to a single species of fermionic particles:

$$K_{\bar{1}} = \hat{p}, \quad A_{\bar{1}} = N - 1, \quad g_{\bar{1}\bar{1}} = 1. \quad (31)$$

The dependence on the pressure profile of the population profile for particles $\bar{1}$ inferred from (6) then becomes

$$\bar{N} = \frac{1}{e^{\hat{p}} + 1}. \quad (32)$$

With (32) substituted into (13), the solution of (14) is

$$\frac{\hat{z}}{2} = \hat{p} + \ln \left(\frac{2}{1 + e^{-\hat{p}}} \right), \quad (33)$$

in analogy to (16) but solved more compactly:

$$\hat{p} = \frac{\hat{z}}{2} - \ln \left(\frac{4}{1 + \sqrt{1 + 8e^{-\hat{z}/2}}} \right). \quad (34)$$

The configurational entropy density derived from (9-10) is recognizably fermionic:

$$\bar{S} = -\bar{N} \ln \bar{N} - (1 - \bar{N}) \ln (1 - \bar{N}) = \frac{\hat{p}}{1 + e^{\hat{p}}} + \ln (1 + e^{-\hat{p}}). \quad (35)$$

The four profiles predicted by configurational statistics for the low-pressure asymptotic regimes are shown in Fig. 4 as the set of curves drawn solid at small \hat{z} and dashed at large \hat{z} . The underlying assumption that tiles 3 and 4 are mechanically stable is accurate near the surface but invalid deep down.

At $\hat{z} \gg 1$ the high gravitational pressure destabilizes practically all tiles 3 and 4 under jamming. This high-pressure asymptotic regime leads us back to the statistical mechanics of scenario (i). If we assume that all tiles 3 and 4 lose mechanical stability at the same threshold pressure p_0 , then we can use Eq. (14) modified into

$$p(z) - p_0 = g \int_{z_0}^z dz' \rho(z'). \quad (36)$$

The solution for scaled variables is

$$e^{\hat{z} - \hat{z}_0} = e^{3(\hat{p} - \hat{p}_0)} \frac{2 + e^{\hat{p}_0} [1 + \sqrt{1 + 4e^{-\hat{p}_0}}]}{2 + e^{\hat{p}} [1 + \sqrt{1 + 4e^{-\hat{p}}}]}. \quad (37)$$

We arrive at the four high-pressure asymptotic profiles shown in Fig. 4 as the set of curves drawn dashed at low \hat{z} and solid at large \hat{z} . The values \hat{z}_0 and \hat{p}_0 are related by the requirement that the pressure be continuous across the point of mechanical instability. For the purpose of illustration we choose $\hat{z}_0 = 4$, implying $\hat{p}_0 \simeq 1.51$,

This oversimplified model of mechanical instability predicts a kink in the pressure profile and discontinuities in the other three profiles. In reality, the mechanical instability of tiles 3 and 4 is a more complex phenomenon as will be discussed next.

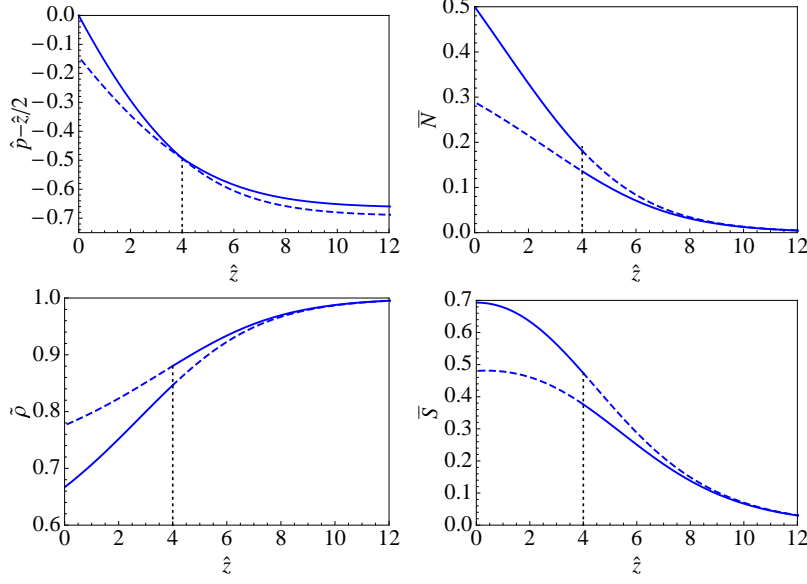


Figure 4. Profiles of scaled pressure, scaled population density of particle tiles, scaled mass density, and scaled entropy, versus scaled depth in the low-pressure asymptotic regime (solid at $\hat{z} < 4$, dashed at $\hat{z} > 4$) and in the high-pressure asymptotic regime (dashed at $\hat{z} < 4$, solid at $\hat{z} > 4$).

5.2. From low to high pressure

Tiles 3 and 4 have conditional mechanical stability. Only a fraction of such tiles that are predicted by configurational statistics to be generated survive jamming. That fraction becomes smaller with increasing pressure.

To describe the physics of this situation most economically we perform the first two mergers (30) of particle tiles. This leads to two species $\bar{1}$ and $\bar{3}$ with specifications $A_{\bar{1}} = N - 1$, $A_{\bar{3}} = 0$, $g_{\bar{1}\bar{1}} = 2$, $g_{\bar{1}\bar{3}} = 1$, $g_{\bar{3}\bar{1}} = -1$, and $g_{\bar{3}\bar{3}} = 0$. Tiles 1 and 2 are represented by particles $\bar{1}$ and tiles 3 and 4 by particles $\bar{3}$.

The population densities of particles $\bar{1}$ and $\bar{3}$ created under local gravitational pressure \hat{p} ,

$$\bar{N}_{\bar{1}}(\hat{p}) = \frac{e^{\hat{p}}}{(1 + e^{\hat{p}})^2}, \quad \bar{N}_{\bar{3}}(\hat{p}) = \frac{1}{(1 + e^{\hat{p}})^2}, \quad (38)$$

are independent of $\hat{\omega}$ because each disk experiences the same centrifugal force.

The ratio $\bar{N}_{\bar{3}}/\bar{N}_{\bar{1}} = e^{-\hat{p}}$ tells us that particles $\bar{3}$ with precarious mechanical stability are already created in lower proportions than the mechanically stable particles $\bar{1}$. That ratio is close to unity at low pressure (near the top) and becomes exponentially small at high pressure (deep down). In fact, both population densities become small at high pressure and the v-tiles become predominant.

In Appendix A.1 we present a model for the conditional mechanical stability of particles $\bar{3}$. It predicts that of the $N_{\bar{3}}$ particles $\bar{3}$ generated at angular velocity $\hat{\omega}$ the fraction that survives jamming under gravitational pressure \hat{p} is

$$R_{\omega}(\hat{p}/\hat{\omega}^2) = \frac{\sigma/d}{\sigma/d + \hat{p}/\hat{\omega}^2}. \quad (39)$$

The limits $R_\omega(0) = 1$ and $R_\omega(\infty) = 0$ represent the physics in the low-pressure and high-pressure asymptotic regimes, respectively.

The total population density of particles $\bar{1}$ and $\bar{3}$ at scaled gravitational pressure \hat{p} and scaled angular velocity $\hat{\omega}$ that survive jamming thus becomes

$$\bar{N}^{(c)}(\hat{p}, \hat{\omega}) \doteq \bar{N}_1(\hat{p}) + R_\omega(\hat{p}/\hat{\omega}^2) \bar{N}_3(\hat{p}) = \frac{R_\omega(\hat{p}/\hat{\omega}^2) + e^{\hat{p}}}{(1 + e^{\hat{p}})^2}, \quad (40)$$

which approaches (32) at low $\hat{p}/\hat{\omega}^2$ and (12) at high $\hat{p}/\hat{\omega}^2$ as required for consistency. Relation (15) now holds for $\hat{z}(\hat{p}, \hat{\omega})$ and $\bar{N}^{(c)}(\hat{p}, \hat{\omega})$.

The four profiles emerging from this more realistic model for the conditional stability of particles $\bar{3}$, now depend on the parameter $\hat{\omega}$, which compares the centrifugal energy of the disks in the spinning channel with the intensity T_k of random agitations used in the jamming protocol. These profiles are shown in the four panels of Fig. 5. All curves are smooth. The singularities predicted by the more primitive model (Fig. 4) have disappeared.

The effects of centrifugal force on the disks in the spinning channel are manifest in the deviations from the dotted curve shown in each panel. Faster spinning stabilizes an increasing number of particles $\bar{3}$. Hence \bar{N} is enhanced. Additional particles produce more disorder, which, in turn, increases \bar{S} . The same particles added, on the other hand, suppress the mass density ρ at the location \hat{z} where they are placed and thus reduce the pressure \hat{p} at any distance \hat{z} measured from the top.

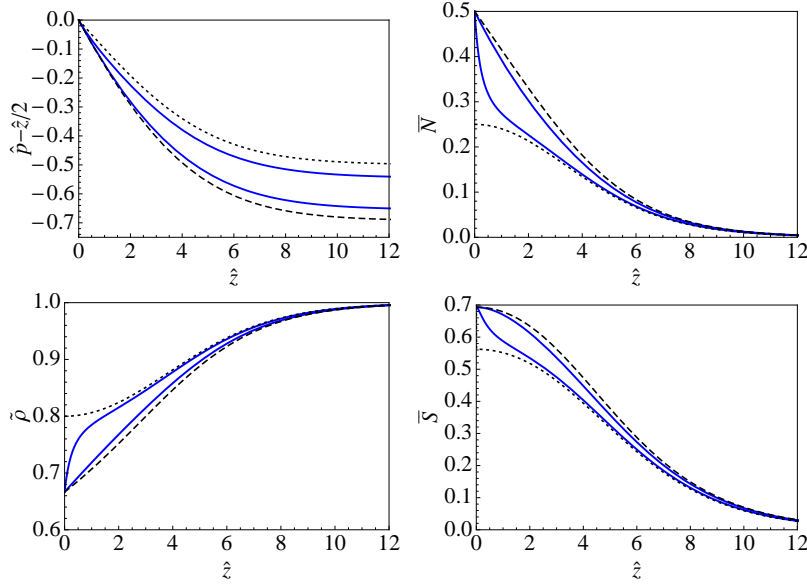


Figure 5. Profiles of scaled pressure, scaled population density of particle tiles, scaled mass density, and scaled entropy, versus scaled depth for scaled angular velocities $\hat{\omega} = \infty$ (dashed line), $\hat{\omega} = 1, 0.2$ (solid lines), and $\hat{\omega} = 0$ (dotted line).

6. Centrifuge with gravity

Physically, scenario (iv) is an extension of scenario (ii). The axis of the channel is horizontal again. Rotation produces centrifugal pressure. The plane of the channel is now vertical with gravity pulling the disks toward the lower wall (see Fig. 1).

Mathematically, scenario (iv) is akin to scenario (iii) but more complex. Only one of the five tiles is mechanically stable at all pressures. The strengths and limitations of configurational statistics are most clearly brought to light in this scenario.

The four familiar profiles depend separately on \hat{p} and \hat{g} , not merely on their ratio. Therefore, the results for light disks and heavy disks cannot be reduced to the same universal curves via scaling. The attributes ‘light’ ($\hat{g} \ll 1$) and ‘heavy’ ($\hat{g} \gg 1$) are gauged by the ratio of the work needed to lift one disk halfway across the channel in units of the intensity of random agitations.

Tiles 2 are mechanically stable and tiles 4 unstable at any pressure. In Appendix A.2 we show that tiles 3 are mechanically stable up to pressure $\hat{p} = \frac{1}{3}\hat{g}$. At higher pressure they are only conditionally stable in the sense that only a fraction of tiles 3 generated by random agitations survive. Conversely, tiles v are unstable at $\hat{p} \leq \frac{1}{3}\hat{g}$ and conditionally stable at $\hat{p} > \frac{1}{3}\hat{g}$. Tiles 1, by contrast, remain unstable up to the higher threshold pressure, $\hat{p} = \frac{2}{3}\hat{g}$, and then become conditionally stable.

For a proper understanding of the physics in this scenario, it is important that we distinguish the balancing of potential energies and the balancing of forces. We first discuss the former, then add the latter to the analysis.

6.1. Competing potential energies

We begin by assuming that all five tiles are mechanically stable at any pressure, meaning that any tile that is generated by random agitations under centrifugal pressure $\hat{p}(\hat{r})$ remains in place when the agitations stop abruptly. In Eqs. (7) the exponents on the left are

$$K_m = \hat{p}(\hat{r}) \pm \hat{g}, \quad (41)$$

where the plus (minus) sign applies to $m = 1, 4$ (2, 3). Their physical solution becomes

$$\begin{aligned} w_1 = w_4 &= e^{\hat{g}} \left[\sqrt{\sinh^2 \hat{g} + e^{2\hat{p}}} + \sinh \hat{g} \right], \\ w_2 = w_3 &= e^{-\hat{g}} \left[\sqrt{\sinh^2 \hat{g} + e^{2\hat{p}}} - \sinh \hat{g} \right], \end{aligned} \quad (42)$$

The tile population densities inferred from (6) are

$$\begin{aligned} \bar{N}_1 = w_1 \bar{N}_4 &= \frac{w_1 w_2}{(1 + w_1)(w_1 + w_2 + 2w_1 w_2)}, \\ \bar{N}_2 = w_2 \bar{N}_3 &= \frac{w_1 w_2}{(1 + w_2)(w_1 + w_2 + 2w_1 w_2)}, \\ \bar{N}_v &\doteq 1 - \sum_{m=1}^4 \bar{N}_m = \frac{2w_1 w_2}{w_1 + w_2 + 2w_1 w_2}. \end{aligned} \quad (43)$$

In Fig. 6 we show these population densities plotted versus \hat{p}/\hat{g} for disks of two different (intermediate) weights. What strikes the eye is the extent to which the results of configurational statistics already reflect the precarious mechanical stability of four of the five tiles.

Tiles 4, which are mechanically unstable at any pressure, are hardly present (less than one in a thousand). Tiles 1, which are unstable at $\hat{p}/\hat{g} < 2/3$, are represented by less than half a percent in that pressure range. At higher pressure, where their stability becomes conditional, their representation remains below one percent.

Tiles \mathbf{v} dominate at high pressure but their population density dips down by a factor of ten at low pressure, where they become unstable. Tiles 3 with complementary stability attributes, dominate at low pressure and virtually disappear at high pressure.

When we increase the weight of the disks by a moderate amount (from $\hat{g} = 1.5$ to $\hat{g} = 2$) the population densities of tiles 1 and 4 experience another significant drop whereas those of tiles \mathbf{v} and 3 reflect their complementary abundance and scarcity in sharper relief. The conversion between tiles \mathbf{v} and 3 is predicted by configurational statistics to take place at $\hat{p}/\hat{g} = 1$ when the scaled compression work \hat{p} is balanced by the scaled gravitational work \hat{g} .

6.2. Competing forces

The mechanical instability involving tiles \mathbf{v} and 3 produces a singularity at $\hat{p}/\hat{g} = \frac{1}{3}$. Below that threshold value all tiles \mathbf{v} spontaneously collapse into tiles 3 due to insufficient centrifugal pressure. This instability is not reflected in the results of Fig. 6.

The competing potential energies come into play while the system is undergoing random agitations and the competing forces that cause mechanical instabilities when the agitations stop and the system is jammed. Configurational statistics naturally accounts for the former. The latter must be imposed in an ad-hoc fashion.

In the current context we proceed by dropping tiles 1 and 4 from consideration, knowing that they are ignorable for $\hat{g} = 1.5$ or higher. In Appendix A.2 we have determined that at $\hat{p}/\hat{g} \leq \frac{1}{3}$ only tiles 3 exist and have estimated that at $\hat{p}/\hat{g} > \frac{1}{3}$ only a fraction,

$$R_g(\hat{p}/\hat{g}) = \frac{\sigma/2d}{\sqrt{1 + \left(\frac{4d}{\sigma} \frac{\hat{p}}{\hat{g}}\right)^2}}. \quad (44)$$

of tiles 3 that are generated survive jamming by centrifugal pressure.

For the population density of tiles 3, corrected to account for their conditional

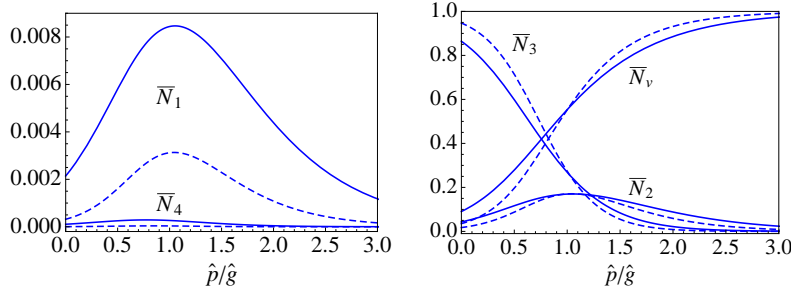


Figure 6. Tile population densities (43) for $\hat{g} = 1.5$ (solid) and $\hat{g} = 2$ (dashed). Note the different vertical scales left and right.

mechanical stability, we thus write

$$\bar{N}_3^{(c)}(\hat{p}, \hat{g}) = \begin{cases} 1, & \hat{p} \leq \frac{1}{3}\hat{g} \\ R_g(\hat{p}/\hat{g}) \frac{\bar{N}_3(\hat{p}, \hat{g})}{\bar{N}_3(\hat{g}/3, \hat{g})}, & \hat{p} > \frac{1}{3}\hat{g} \end{cases}, \quad (45)$$

where $\bar{N}_3(\hat{p}, \hat{g})$ comes from (43).

This expression takes into account that configurational statistics underestimates the number of tiles 3 near the mechanical instability. The correction has the consequence that the number of tiles 3 are overestimated by the same factor at high \hat{p} , where configurational statistics is more accurate. The side effect is negligible because the number of tiles 3 decreases rapidly as \hat{p} increases from the point of instability.

Contrary to what configurational statistics predicts (see Fig. 6), there are no tiles v and 2 at $\hat{p}/\hat{g} \leq \frac{1}{3}$. As the centrifugal pressure decreases toward the point of mechanical instability, $\hat{p}/\hat{g} = \frac{1}{3}$, tiles v collapse into tiles 3 and convert 2 into tiles 3 in the process. That conversion is best captured in the following corrected population density of tiles 2:

$$N_2^{(c)}(\hat{p}, \hat{g}) = [1 - N_3^{(c)}(\hat{p}, \hat{g})]N_2(\hat{p}, \hat{g}). \quad (46)$$

The corrected population densities of tiles v is then the complement,

$$N_v^{(c)}(\hat{p}, \hat{g}) = 1 - N_2^{(c)}(\hat{p}, \hat{g}) - N_3^{(c)}(\hat{p}, \hat{g}). \quad (47)$$

By avoiding any direct manipulation of $N_v(\hat{p}, \hat{g})$ we minimize the effects at high pressure of our approximate accounting for the mechanical instability. In Fig. 7 we show the three population densities corrected for the presence of the mechanical instability in comparison with their uncorrected counterparts for two values of \hat{g} .

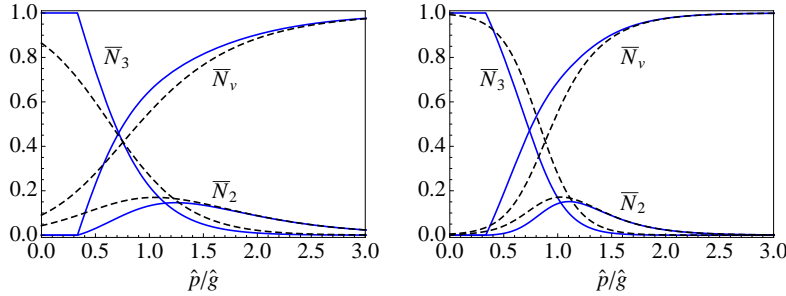


Figure 7. Population densities of tiles v, 2, and 3 versus \hat{p}/\hat{g} for $\hat{g} = 1.5$ (left) and $\hat{g} = 3$ (right). The dashed lines represent the results (43). The solid lines account for the mechanical instability at $\hat{p}/\hat{g} = \frac{1}{3}$ via the results (45)-(47).

We see that the effects of the mechanical instability do indeed have no significant impact at high pressure as should be the case. We also discern parallel trends (most clearly for $\hat{g} = 3$) produced by the competing potential energies at $\hat{p}/\hat{g} = 1$ in the uncorrected results and the competing forces at $\hat{p}/\hat{g} = \frac{1}{3}$ in the corrected results.

For the calculation of the four profiles we must use relation (27) now relating $\hat{r}(\hat{p}, \hat{g})$ to $\bar{N}(\hat{p}, \hat{g})$, where $\bar{N}(\hat{p}, \hat{g})$ is the sum of all four population densities in the uncorrected results and the sum of $N_2^{(c)}(\hat{p}, \hat{g})$ and $N_3^{(c)}(\hat{p}, \hat{g})$ in the results corrected for the mechanical instability.

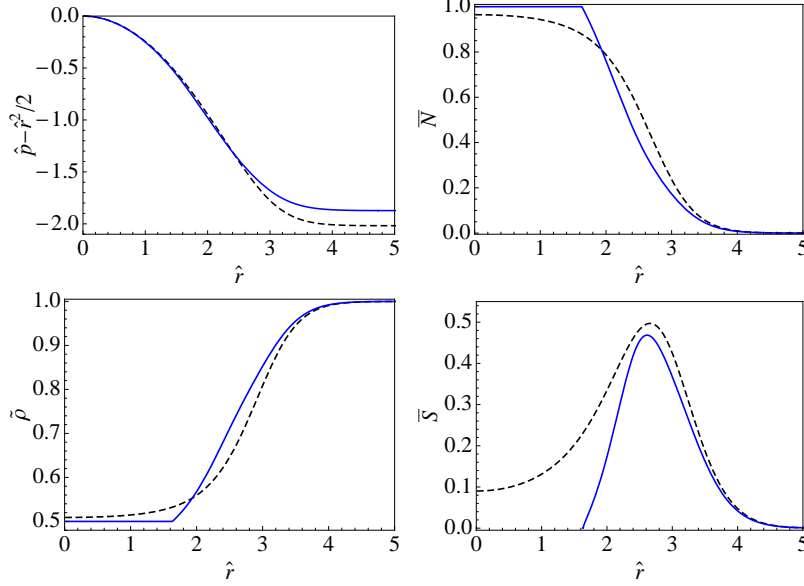


Figure 8. Profiles of scaled pressure, scaled population density of particle tiles, scaled mass density, and scaled entropy, versus scaled radius in scenario (iv) with $\hat{g} = 2$. The dashed lines represent the results that account only for statistical instabilities. The solid lines also account for the mechanical instability at $\hat{p}/\hat{g} = \frac{1}{3}$.

In Fig. 8 we show these four profiles for the case $\hat{g} = 2$. The dashed curves highlight the effect of competing potential energies at $\hat{p}/\hat{g} = 1$, whereas the solid curves also include the effects of the competing forces (mechanical instability) at $\hat{p}/\hat{g} = \frac{1}{3}$.

7. Conclusion

External fields produce characteristic profiles for local pressure, mass density, entropy density, and other properties of granular matter. These profiles may vary sufficiently slowly to be ignorable under many circumstances, but they are real. Our study suggests that these profiles are generated in two stages.

(i) While the random agitations are in operation, configurations of granular particles are being weighted, in a first selection process, according to competing potential energies due to contact forces and external forces.

(ii) When the random agitations stop and a jammed microstate is frozen out, a second selection process eliminates configurations that are mechanically unstable.

The evidence for these profiles resulting from a two-stage jamming process pertains, admittedly, to an idealized system of disks confined to a narrow channel subjected to gravity or centrifuge or both. However, the scouting for clues to a deeper understanding of multifaceted processes in complex systems via studies of idealized scenarios that can be analyzed with some rigor is an accepted practice with documented success in granular matter studies [20, 21, 22, 23, 24, 25] and elsewhere.

Finally, we wish to comment on a series of theoretical studies by Luck and Mehta [26-30] that investigate columns of grains in jammed configurations with trapped void spaces. The methodology is quite different from ours, based on a stochastic process

for transitions between discrete states of individual grains with different degrees of ordering. The model transition rates depend on three parameters: (i) the intensity of vibrations akin to our T_k , assumed uniform as in our study; (ii) a scaled activation energy, akin to our \hat{p} , that grows with depth and slows down transitions with increasing depth; (iii) a local ordering field that controls the presence of trapped voids at given depth. In our approach, this last task is assumed by the statistically interacting tiles with activation energies that depend on depth. It will be interesting to compare the results of the two approaches once our methodology has been extended to include the kinetics of transitions between different tile configurations.

Appendix A. Mechanical instabilities

Here we examine the statistical effects of mechanical instabilities of tiles under conditions realized in two scenarios.

Appendix A.1. Scenario (iii)

Two disks touching the same wall, held in place by disks touching the opposite wall, represent a tile $\bar{1}$. It has unconditional mechanical stability. A configuration with three or more disks touching the same wall involves at least one tile $\bar{3}$. Its mechanical stability depends on the strength of the centrifugal force at given local gravitational pressure.

Configurational statistics predicts expressions (38) for the population densities of tiles $\bar{1}$ and $\bar{3}$ under the assumption that the mechanical stability of all tiles is unconditional. These tiles are generated by random agitations of given intensity.

For an estimate of the fraction R_ω of tiles $\bar{3}$ that survive jamming, we consider the configuration depicted on the left of Fig. A1. Tiles $\bar{3}$ have a chance to be generated if three consecutive disks are positioned on the same side of the channel with the middle one closer to the center (dot-dashed line).

The stabilizing centrifugal force depends on the distance of the middle disk from the central axis. The destabilizing force depends on the local pressure and the relative horizontal position of the middle disk to its two neighbors. The additional assumption that both outer disks touch the wall has only a mild impact on the estimate but simplifies the calculation significantly.

The stabilizing and destabilizing forces are in balance if the middle disk is at position

$$c = \frac{\hat{p}}{\hat{\omega}^2} d \tan \phi_c \simeq \frac{\hat{p}}{\hat{\omega}^2} d \sin \phi_c, \quad (\text{A.1})$$

where we take into account that the angle ϕ_c is small.

The fraction of three-disk configurations shown that lead to tiles $\bar{3}$ under jamming is then estimated to be

$$R_\omega = \frac{d - c}{d}, \quad (\text{A.2})$$

which, in conjunction with (A.1), exhibits the following dependence on the stabilizing agent $\hat{\omega}$ and the destabilizing agent \hat{p} :

$$R_\omega(\hat{p}/\hat{\omega}^2) = \frac{\sigma/d}{\sigma/d + \hat{p}/\hat{\omega}^2}. \quad (\text{A.3})$$

This function, plotted in Fig. A1, is used in the analysis of Sec. 5.2.

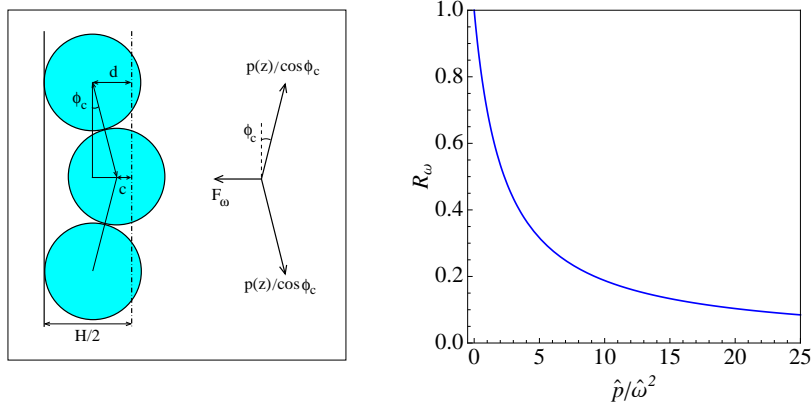


Figure A1. Three-disk configuration with the stabilizing centrifugal force $F_\omega \doteq \mu\omega^2 c$ balancing the destabilizing contact forces $p(z)/\cos\phi_c$ (left). Fraction R_ω of tiles 3 predicted to be mechanically stable as a function of $\hat{p}/\hat{\omega}^2$ (right).

Appendix A.2. Scenario (iv)

Two disks touching the bottom wall, held in place by disks touching the top wall, represent a tile 2. It has unconditional mechanical stability. A configuration with three or more disks touching the bottom wall contains at least one tile 3. Its mechanical stability depends on the strength of the local centrifugal pressure in relation to the weight of the disk.

Configurational statistics predicts population densities (43) under the assumption that the mechanical stability of all tiles is unconditional. Here we estimate the fraction R_g of tiles 3 that survive jamming by centrifugal pressure.

We consider the configuration depicted on the left of Fig. A2. Tiles 3 have a chance to be generated if three consecutive disks are positioned near the bottom of the channel with the middle one furthest from the wall before jamming begins. The effectiveness of the stabilizing weight of the middle disk depends on the local pressure

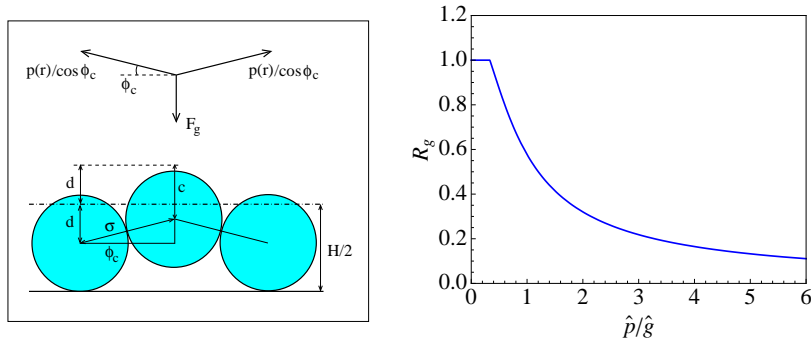


Figure A2. Three-disk configuration with the stabilizing gravitational force $F_g \doteq \mu g$ in balancing the destabilizing contact forces $p(r)/\cos\phi_c$ (left). Fraction R_g of tiles 3 predicted to be mechanically stable as a function of \hat{p}/\hat{g} (right).

and the relative vertical position of the middle disk relative to its two neighbors. As before we argue that the impact of additional assumptions is ignorable.

The stabilizing and destabilizing forces are in balance if the middle disk is at position c , implying

$$\cot \phi_c = \frac{4d}{\sigma} \frac{\hat{p}}{\hat{g}}. \quad (\text{A.4})$$

The parameter \hat{p}/\hat{g} varies along the channel in a controlled way. The fraction of three-disk configurations shown that lead to tiles 3 under jamming is

$$R_g = \frac{2d - c}{2d}, \quad (\text{A.5})$$

from which we infer the function

$$R_g(\hat{p}/\hat{g}) = \frac{\sigma/2d}{\sqrt{1 + (4d\hat{p}/\sigma\hat{g})^2}}. \quad (\text{A.6})$$

The ratio levels off in a cusp at $\hat{p}/\hat{g} = \frac{1}{3}$ when it reaches unity as shown in Fig. A2.

References

- [1] D. Frenkel in *Understanding soft condensed matter via modeling and computation*, W. Hu and A.-C. Shi (Eds.), World Scientific, Singapore (2011).
- [2] C. O'Hern, S. A. Langer, A. J. Liu, and S. R. Nagel, Phys. Rev. Lett. **88**, 075507 (2002).
- [3] T. S. Majumdar, M. Sperl, S. Luding, and R. P. Behringer, Phys. Rev. Lett. **98**, 058001 (2007).
- [4] D. A. Head, Phys. Rev. Lett. **102**, 138001 (2009).
- [5] M. Schröter, S. Nägele, C. Radin, and H. L. Swinney, EPL, **78**, 44004 (2007).
- [6] P. Charbonneau, E. I. Corwin, G. Parisi, and F. Zamponi, Phys. Rev. Lett. **109**, 205501 (2012).
- [7] C. Song, P. Wang, and H. A. Makse, Nature **453**, 625 (2008).
- [8] C. Briscoe, C. Song, P. Wang, and H. A. Makse, Phys. Rev. Lett. **101**, 188001 (2008).
- [9] C. Briscoe, C. Song, P. Wang, and H. A. Makse, Physica A **389**, 3978 (2010).
- [10] Y. Jin and H. A. Makse, Physica A **389**, 5362 (2010).
- [11] P. Wang, C. Song, Y. Jin, and H. A. Makse, arXiv:0808.2196.
- [12] M. P. Ciamarra, R. Pastore, M. Nicodemi, and A. Coniglio, Phys. Rev. E **84**, 041308 (2011).
- [13] S. Meyer, C. Song, Y. Jin, K. Wang, and H. A. Makse, Physica A **389**, 5137 (2010).
- [14] B. D. Lubachevsky and F. H. Stillinger, J. Stat. Phys. **60**, 561 (1990).
- [15] T. Unger, J. Kertesz, and D. E. Wolf, Phys. Rev. Lett. **94**, 178001 (2005).
- [16] J. Zhang, T. S. Majumdar, M. Sperl, and R. P. Behringer, Soft Matter **6**, 2982 (2010).
- [17] K. W. Desmond and E. R. Weeks, Phys. Rev. E **80**, 051305 (2009).
- [18] G.-J. Gao, J. Blawdziewicz, C. S. O'Hern, and M. Shattuck, Phys. Rev. E **80**, 061304 (2009).
- [19] S. S. Ashwin, J. Blawdziewicz, C. S. O'Hern, and M. D. Shattuck, Phys. Rev. E **85**, 061307 (2012).
- [20] R. K. Bowles and I. Saika-Voivod, Phys. Rev. E **73**, 011503 (2006).
- [21] S. S. Ashwin and R. K. Bowles, Phys. Rev. Lett. **102**, 235701 (2009).
- [22] R. K. Bowles and S. S. Ashwin, Phys. Rev. E **83**, 031302 (2011).
- [23] N. Gundlach, M. Karbach, D. Liu, and G. Müller, J. Stat. Mech. **P04018** (2013).
- [24] M. Z. Yamchi, S. S. Ashwin, and R. K. Bowles, Phys. Rev. Lett. **109**, 225701 (2012).
- [25] S. S. Ashwin, M. Z. Yamchi, and R. K. Bowles, Phys. Rev. Lett. **110**, 145701 (2013).
- [26] P. F. Stadler, J. M. Luck, and A. Mehta, Eur. Phys. Lett. **57**, 46 (2001).
- [27] J. M. Luck and A. Mehta, Eur. Phys. J. B **35**, 399 (2003).
- [28] A. Mehta and J. M. Luck, J. Phys. A: Math. Gen. **36**, L365 (2003).
- [29] J. M. Luck and A. Mehta, Eur. Phys. J. B **57**, 429 (2007).
- [30] J. M. Luck and A. Mehta, Euro. Phys. J. B **77**, 505 (2010).
- [31] F. D. M. Haldane, Phys. Rev. Lett. **67**, 937 (1991).
- [32] Y.-S. Wu, Phys. Rev. Lett. **73**, 922 (1994).
- [33] S. B. Isakov, Phys. Rev. Lett. **73**, 2150 (1994); Mod. Phys. Lett. B **8**, 319 (1994).
- [34] D.-V. Anghel, J. Phys. A **40**, F1013 (2007); Europhys. Lett. **87**, 60009 (2009).
- [35] P. Lu, J. Vanasse, C. Piecuch, M. Karbach, and G. Müller, J. Phys. A **41**, 265003 (2008).
- [36] D. Liu, P. Lu, G. Müller, and M. Karbach, Phys. Rev. E **84**, 021136 (2011).

- [37] P. Lu, D. Liu, G. Müller, and M. Karbach *Condens. Matter Phys.* **15**, 13001 (2012).
- [38] D. Liu, J. Vanasse, G. Müller, and M. Karbach, *Phys. Rev. E* **85**, 011144 (2012).
- [39] S. F. Edwards and R. B. S. Oakeshott, *Physica A* **157**, 1080 (1989).
- [40] A. Mehta and S. F. Edwards, *Physica A* **157**, 1091 (1989).